Monthly Notices of the ROYAL ASTRONOMICAL SOCIETY
MNRAS Advance Access published March 11, 2014
MNRAS (2014) doi:10.1093/mnras/stu293

Analysis of single pulse radio flux measurements of PSR B1133+16 at 4.85 and 8.35 GHz

K. Krzeszowski,[1★] O. Maron,[1] A. Słowikowska,[1] J. Dyks[2] and A. Jessner[3]

[1]Kepler Institute of Astronomy, University of Zielona Góra, Lubuska 2, PL-65–265 Zielona Góra, Poland
[2]Nicolaus Copernicus Astronomical Center, Rabiańska 8, PL-87-100 Toruń, Poland
[3]Max-Planck-Institut für Radioastronomie, Auf dem Hügel 69, D-53121 Bonn, Germany

Accepted 2014 February 11. Received 2014 February 7; in original form 2013 November 8

ABSTRACT

We show the results of microsecond resolution radio data analysis focused on flux measurements of single pulses of PSR B1133+16. The data were recorded at 4.85 and 8.35 GHz with 0.5- and 1.1-GHz bandwidth, respectively, using Radio Telescope Effelsberg (Max-Planck-Institut für Radioastronomie). The most important conclusion of the analysis is that the strongest single pulse emission at 4.85 and 8.35 GHz contributes almost exclusively to the trailing part of the leading component of the pulsar mean profile, whereas studies at lower frequencies report that the contribution is spread almost uniformly, covering all phases of the pulsar mean profile. We also estimate the radio emission heights to be around 1–2 per cent of the light-cylinder radius, which is in agreement with previous studies. Additionally, these observations allowed us to add two more measurements of the flux density to the PSR B1133+16 broad-band radio spectrum, covering frequencies from 16.7 MHz up to 32 GHz. We fit two different models to the spectrum: a broken power law and a spectrum based on the flicker-noise model, which represents the spectrum in a simpler, but similarly accurate, way.

Key words: pulsars: general – pulsars: individual: B1133+16.

1 INTRODUCTION

Pulsar radio emission is still not explained in detail, but it is believed to originate close to the pulsar surface (see Krzeszowski et al. 2009, and references therein). The analysis of 62 mean profiles of 23 pulsars at different frequencies regarding aberration and retardation effects yielded an estimation of the emission height that is certainly below 1500 km, but most probably of the order of 500 km above the pulsar surface. Advances in theoretical understanding of the emission mechanism and conditions in the magnetosphere have been driven mainly by observations. Recently, many observations have concentrated on observing single pulses, which carry detailed information about the physics of radio emission. Analysis of single pulse high-resolution time series can show a few interesting properties, such as giant and bright pulses, subpulse drift, nulling, microstructure, etc. Observations of single pulses for most pulsars may be carried out mainly at lower frequencies, because pulsars are weak radio sources at high frequencies, which is clearly seen in their steep spectra. The pulsar spectrum in general can be described by a power law $S \propto \nu^{\alpha}$, where α is the spectral index. The average spectral index for 266 pulsars for frequency spread 0.4–23 GHz is $\alpha = -1.8$ (Maron et al. 2000).

PSR B1133+16 is a nearby middle-aged pulsar with one of the highest proper motions and thus the highest transverse velocity (Brisken et al. 2002). The basic properties of PSR B1133+16 are gathered in Table 1. Its faint optical counterpart ($B = 28.1 \pm 0.3$ mag) was first detected by Zharikov et al. (2008). Recently, Zharikov & Mignani (2013) detected an optical candidate of the pulsar counterpart in Gran Telescopio Canarias (GTC) and Very Large Telescope (VLT) images that is consistent with the radio coordinates corrected for its proper motion. This source was also detected in X-rays by Kargaltsev, Pavlov & Garmire (2006) using the *Chandra* satellite, with a flux of $(0.8 \pm 0.2) \times 10^{-14}$ erg cm^{-2} s^{-1} in the 0.5–8.0 keV range. For the X-ray fit, the assumed hydrogen column density was $n_{\rm H} = 1.5 \times 10^{20}$ cm^{-2}. The low value of $n_{\rm H}$ and lack of Hα Balmer bow shock imply a low density of ambient matter around the pulsar. This pulsar has not been detected by the *Fermi* satellite.

In this article, in Section 2 we describe observational parameters and technical issues regarding the recorded data. Section 3 covers analysis of the data. We present two different approaches for data analysis: mean profiles composed of pulses with flux falling into a specific intensity range and also the phase position and flux of single pulses that are stronger than 20σ. In Section 4 we discuss radio emission height estimations, while in Section 5 we present the radio spectrum of PSR B1133+16 and discuss different spectrum models. We conclude in Section 6.

★ E-mail: chriss@astro.ia.uz.zgora.pl

Published by Oxford University Press on behalf of the Royal Astronomical Society

Table 1. Basic properties of PSR B1133+16 (Brisken et al. 2002; Manchester et al. 2005).

BNAME	B1133+16
JNAME	J1136+1551
P	1.188 s
$\dot{P}$	3.73×10^{-15} s s^{-1}
RA (J2000)	$11^{\mathrm{h}}36^{\mathrm{m}}03^{\mathrm{s}}$
Dec. (J2000)	$15°51'04''$
DM	4.86 pc cm^{-3}
RM	1.1 rad m^{2}
Age	5.04×10^{6} yr
Distance	350 ± 20 pc
Proper motion	375 mas yr^{-1}
Transverse velocity	631^{+38}_{-35} km s^{-1}
B_{surf}	2.13×10^{12} G
$\dot{E}$	8.8×10^{31} erg s^{-1}

Table 2. Observation parameters.

Date	2002 Feb 07	2004 Apr 26
Frequency	4.85 GHz	8.35 GHz
Bandwidth	0.5 GHz	1.1 GHz
Observing time	67 min	120 min
Number of pulses	3361	6029
Sampling time	200 µs	60 µs
Mean flux density	1.59 mJy	0.73 mJy

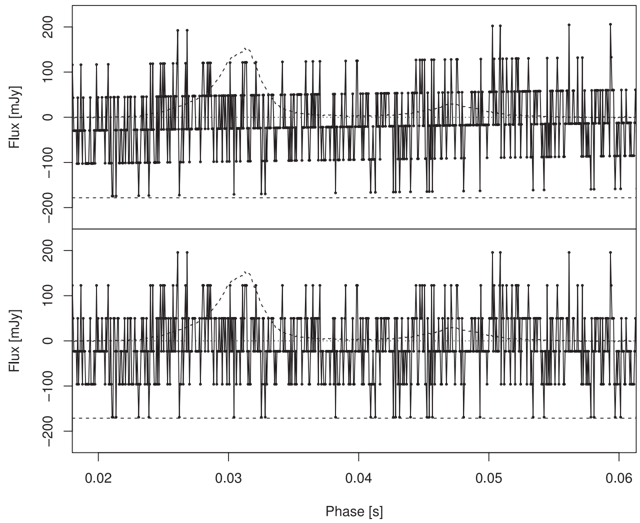

Figure 1. Weak single pulse of PSR B1133+16 at 8.35 GHz with a visible linear trend (top panel) and after correction (bottom panel). The mean profile (dashed line) is plotted for comparison. The horizontal dashed line is shown for reference.

2 OBSERVATIONS AND DATA REDUCTION

Our analysis is based on the Radio Telescope Effelsberg archival data. The observational settings and parameters are collected in Table 2. Observations were made using the 4.85- and 8.35-GHz receivers of the Max-Planck-Institut für Radioastronomie (MPIfR) 100-m radio telescope in Effelsberg. The receivers have circularly polarized feeds. Both receivers feature cryogenically cooled high-electron-mobility transistor (HEMT) low-noise input stages with typical system temperatures of 27 K for the 4.85-GHz receiver and 22 K for the 8.35-GHz receivers. A calibration signal can be injected synchronously to the pulse period for accurate measurements of pulsar flux densities. The Effelsberg radio telescope is regularly calibrated on catalogued continuum sources and we used the mean height of the injected calibration signal of 1.2 K for 4.85 GHz and 2.083 K for 8.35 GHz for the flux calibrations. The two intermediate-frequency (IF) signals (bandwidths of 500 MHz for 4.85 GHz and 1.1 GHz for 8.35 GHz) from each receiver, one for left-hand (LHC) and one for right-hand (RHC) circular polarization, are detected in a broad-band polarimeter attached to the receiver, providing four output-independent signals relating to the power levels of LHC, RHC, LHC·RHC· sin (LHC,RHC) and LHC·RHC· cos (LHC,RHC). No dedispersion was used before or after the detection, due to the low value of Dispersion Measure (DM) of PSR B1133+16. The dispersion broadening amounts to 178 and 78 µs for 4.85 and 8.35 GHz, respectively, which is of the order of the sampling rates. The four detected power levels are linearly encoded as short pulses of variable frequency, typically 2–3 MHz, corresponding to the system noise level, but ranging up to a maximum of 10 MHz. These signals were brought down to the station building and, using the Effelsberg Pulsar Observation System (EPOS) backend, the four frequency-encoded power levels were recorded synchronously to the pulse period in 1024 phase bins (=samples) per period. The average signal power for each phase bin was determined by simply counting the number of pulses of the supplied frequency-encoded signal for the duration of the phase bin and then recording the counts on disk for later off-line processing. Only data from LHC and RHC channels were used and added together to yield the detected total power for our analysis. The individual phase bins had durations of 200 µs for 4.85 GHz and 60 µs for 8.35 GHz. With the given system temperatures and the respective antenna efficiencies of 1.5 and 1.2 K Jy^{-1}, we achieved typical sensitivities (rms) of 30 and 80 mJy per single pulse phase bin for the two frequencies, respectively.

2.1 Digitization effects

The aforementioned sensitivity corresponds to a fraction of 2–3×10^{-3} of the equivalent background (baseline) noise level of 16–18 Jy. At the same time, we recorded typically only 600 (4.85 GHz) down to 200 (at 8.35 GHz) frequency-encoded counts per phase bin. As a result, one finds that the signal power is resolved in steps of 30 and 80 mJy for the two receivers and that the rms noise fluctuations are barely resolved, amounting to a couple of counts at most (see Fig. 1).

2.2 Weather and radio interference

Weather, especially clouds, changes the opacity of the atmosphere and as a consequence we found that fluctuations of the sky background were of the order of a fraction of a K on the short time-scales (200 and 60 ms) used for the measurement window and the subtraction of the noise baseline. Both receivers were also affected by a very low-level 100 Hz modulation (10^{-3}–10^{-4} of the baseline level) originating in the receiver's power supply and cooling systems. With typical observed pulse component widths of 5–10 ms, we find that we cannot rule out that weak individual components of individual single pulses may be affected by the interference. However, averaging and other statistical flux estimates using sufficient numbers (>10) of single pulses would not be affected by weather-induced noise fluctuations or power-supply interference.

The above-mentioned effects are visible in the data as approximately linear trends added to each of the recorded single pulses. One example of such a slope and effects of the correction at 8.35 GHz

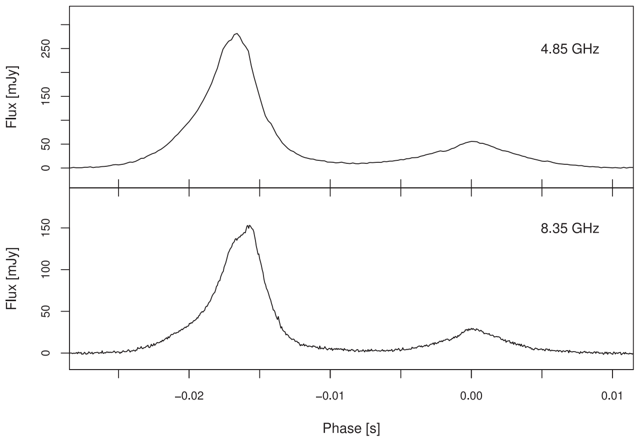

Figure 2. Mean profiles of PSR B1133+16 at 4.85 GHz (top panel) and 8.35 GHz (bottom panel). The profiles are aligned with respect to the maximum of the trailing component.

is presented in Fig. 1. The values of the slopes show no trends from pulse to pulse and range from −2 to 2 mJy bin^{-1}; their distribution is a Gaussian-like with a zero mean. The behaviour of the system at 4.85 GHz is roughly the same as that of 8.35-GHz data and the same correction routines were applied.

3 SINGLE PULSES IN MICROSECOND RESOLUTION

Average profiles of PSR B1133+16 at 4.85 and 8.35 GHz consist of two main components connected by a bridge of emission (Fig. 2). The leading component is approximately five times stronger than the trailing one and they are separated by around 5°. The duty cycle of this pulsar is around 3 per cent at 4.85 and 8.35 GHz.

We performed an analysis of microsecond-resolution radio data focused on flux measurements of single pulses. High-resolution observations allowed us to investigate the microstructure of single pulse shapes. The single pulse at 8.35 GHz in the top panel of Fig. 3 shows interesting features in the trailing component. On the other hand, the bottom panel of Fig. 3 is focused on the leading component of another single pulse profile at the same frequency. As can be clearly seen, single pulse profiles have complex structures, which can be resolved only with high time resolution observations. There have been numerous studies of the microstructure of PSR B1133+16 and other pulsars (e.g. Ferguson & Seiradakis 1978; Lange et al. 1998). It is reported that microstructure is most probably related to the emission process and is present in many pulsars, with the fraction of pulses showing microstructure being of the order of 30–70 per cent (Lange et al. 1998).

3.1 Time-scale constraints on geometrical parameters

The time-scale of real-time flux variability (such as the micro- or nanostructure) can be interpreted in terms of the size of the emitting region or the angular size of the relativistically beamed radiation pattern (Lange et al. 1998; Crossley et al. 2010). The outcome depends on the actual spatial and temporal structure of the emission region and its relation to the angular scale of the radiated beam.

Let us consider a localized and relativistically outflowing source of radio emission, e.g. a cloud of charges with Lorentz factor γ moving along a *narrow* bunch of magnetic field lines. Here, *narrow* means that the spread of B-field direction within the emitting stream, as measured for different rotational azimuths, is smaller than the intrinsic size of the emission pattern $1/\gamma$. In the observer's reference frame, the charges move along a narrow bunch of trajectories with radius of curvature ρ. If the source emits detectable radiation for a limited period of time $\Delta t_{\rm em}$ (as measured in our reference frame), an observed spike of radio flux has a width $\tau \equiv \Delta t_{\rm obs} = \Delta t_{\rm em}(c - v)/c \simeq \Delta t_{\rm em}/(2\gamma^2)$ (since the outflowing source is nearly catching up with the emitted photons). If the source persists for a time sufficient to sweep its full $1/\gamma$ beam across the observer's line of sight, then $\Delta t_{\rm em} \simeq \rho/(\gamma c)$ and the time-scale is

$$\tau = \tau_\rho \simeq \rho/(2c\gamma^3) = 1.7 \times 10^{-9}{\rm s}\ \rho_8/\gamma_2^3, \quad (1)$$

where $\rho_8 = \rho/10^8$ cm and $\gamma_2 = \gamma/100$ (Jackson 1975). During that time, the point source moves up in the pulsar magnetosphere by a distance $c\Delta t_{\rm em} \simeq 10^6 {\rm cm}\ \rho_8/\gamma_2$. For $\rho = 10^8$ cm, the observed time-scale of the microstructure of $\tau \sim 100$ µs limits the Lorentz factor to the mildly relativistic value $\gamma \simeq 2.6$. For $\gamma = 10$, the observed time-scale implies $\rho \simeq 6 \times 10^9$ cm, comparable to the light-cylinder radius of PSR B1133+16 ($R_{\rm LC} = 5.67 \times 10^9$ cm). Note that for the curvature radiation from a localized emitter, by definition one expects $\tau \simeq 1/\nu$, where ν is the observed frequency (a few GHz). That is, the pair of values ρ and γ must ensure that the curvature spectrum extends up to the frequency ν. The observed time-scale of the microstructure ($\sim 10^{-4}$ s) is then too long to correspond directly to the rapid sweep of the elementary beam of the curvature radiation emitted by a small plasma cloud.

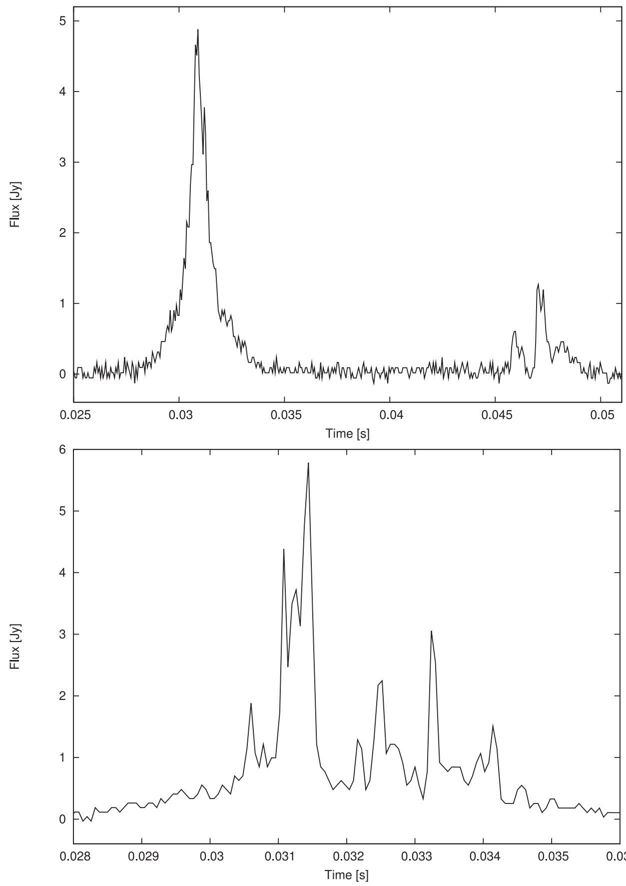

Figure 3. An example of a strong single pulse of PSR B1133+16 at 8.35 GHz with some interesting features in the trailing component (top panel) and the structure of the leading component of another strong single pulse profile at 8.35 GHz (bottom panel).

Another case is encountered when the emitting clouds extend considerably along B-field lines ($\Delta x \gg \rho\gamma^{-3}$) or when there is a steady outflow of uniformly distributed matter that emits radio waves. Again, let us first consider the *narrow stream* case, in which the internal spread of rotational azimuths $\Delta\phi_B$ of $\boldsymbol{B}$ is much smaller than the size of the relativistic beam ($\Delta\phi_B \ll 1/\gamma$). In such a case, projection of the beam on the sky results in an elongated stripe of width $1/\gamma$. The observed time-scale is then determined by the speed of sightline passage through the $1/\gamma$ stripe, as resulting from the rotation of the neutron star:

$$\tau = \tau_{\rm rot} \simeq P\,(2\pi\gamma\,\sin\zeta\,\sin\delta_{\rm cut})^{-1}$$

$$= 1.6 \times 10^{-3} P\,(\gamma_2 \sin\zeta\,\sin\delta_{\rm cut})^{-1}, \qquad (2)$$

where ζ is the viewing angle between the sightline and the rotation axis and $\delta_{\rm cut}$ is the 'cut angle' between the sky-projected emission stripe and the path of the line of sight while it is traversing through the beam (see fig. 2 in Dyks & Rudak 2012). Lange et al. (1998) provide a similar time-scale estimate (equation 6 therein), which is valid only for $\delta_{\rm cut} = 90°$, i.e. for orthogonal passage of the sightline through the beam. For the parameters $\alpha = 88°$ and $\zeta = 97°$ determined by Gangadhara et al. (1999), the observed separation of components ($2\phi \simeq 5°$) implies $\delta_{\rm cut} = 74°$. Equation (2) then gives $\gamma_2 \simeq 20$, which is smaller than the minimum Lorentz factor required for the curvature spectrum to extend up to the observed frequency of a few GeV.

In a thick stream case, the spread of rotational azimuths of $\boldsymbol{B}$ within the stream is much larger than the angular size of the stream ($\Delta\phi_B \gg 1/\gamma$). The emitted radiation can be considered (approximately) tangent to the local magnetic field and to the charge trajectory in the observer's frame. The observed time-scale is then determined by the angular extent of the stream in the magnetic azimuth $\phi_{\rm m}$, measured around the dipole axis. For the stream extending between $\phi_{\rm m,1}$ and $\phi_{\rm m,2}$, the time-scale is equal to $\tau = \tau_{\phi{\rm m}} = \phi_2 - \phi_1$, where the pulse longitudes $\phi_1(\phi_{\rm m,1})$ and $\phi_2(\phi_{\rm m,2})$ correspond to the moments when our sightline starts and stops probing the region of the stream. For known (or assumed) α, ζ, $\phi_{\rm m,1}$ and $\phi_{\rm m,2}$, the values of ϕ_1 and ϕ_2 can be calculated from equations (18) and (19) in Dyks, Rudak & Demorest (2010). However, the time-scale $\tau \sim 100\,\mu$s corresponds to angle $2\pi\tau/P = 0.03°$, which requires $\gamma \geq 2 \times 10^3$. Thus, for PSR B1133+16 the thick stream case may need to be considered only for $\gamma >$ a few thousand.

3.2 Single pulse flux distribution

We define bright pulses as those with energy ten times greater than the mean flux of the pulsar. Looking closer at the flux density distribution (Fig. 4), one can see that there are not many bright pulses in our time series, only around 0.9 per cent at both frequencies.

All flux measurements (Fig. 4) for both frequencies were divided into ten equally sized intensity ranges (Nowakowski 1996). The ranges were constructed as follows: the minimum and maximum flux measurements from each data set were taken as boundaries and all remaining pulse flux values were assigned to one of the $(S_{\rm max} - S_{\rm min})/10$ ranges of widths around 5 and 3 mJy for 4.85 and 8.35 GHz, respectively. The minimum and maximum flux values are -0.83 and 53.11 mJy as well as -1.38 and 27.15 mJy for 4.85 and 8.35 GHz data, respectively. Negative flux values are introduced into the data because of observing-system properties, which were discussed in detail in Section 2, and stochastic noise properties in pulses with no detection. For the single pulses with flux falling into a

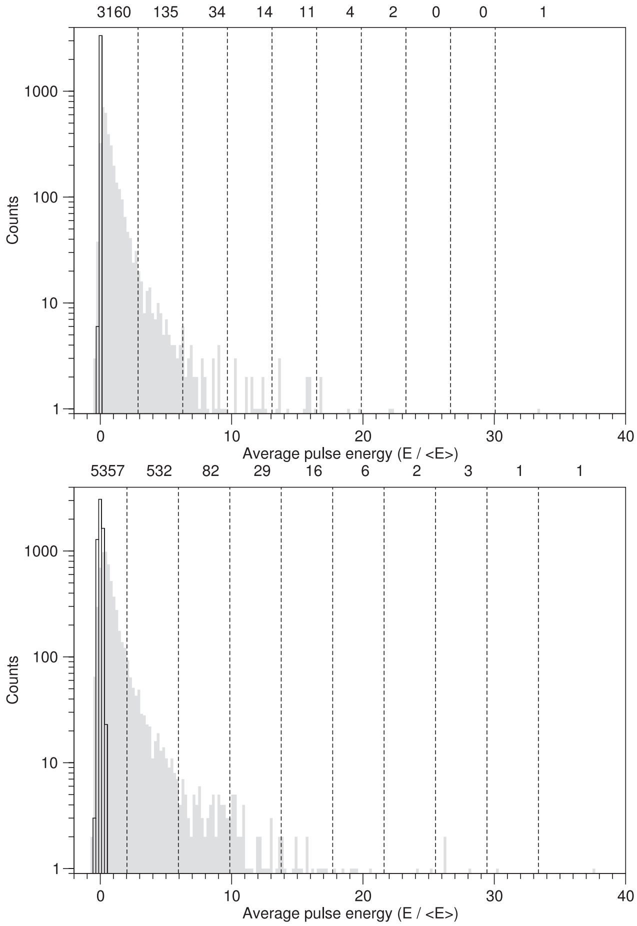

Figure 4. Flux density distribution (grey bars) and off-pulse intensity distribution (black outlined bars) of 4.85 GHz (top panel) and 8.35 GHz (bottom panel) data. Vertical dashed lines denote ten intensity ranges with the number of pulses that fall into that particular range. Mean profiles composed of single pulses that fall into a particular range are presented in Fig. 5 for both frequencies.

particular range, the average profiles were constructed. Normalized profiles for 4.85- and 8.35-GHz data and respective mean profiles of the first five intensity ranges are presented in Fig. 5. The number of pulses falling into specific intensity range is written in each panel and also shown in Fig. 4 above the distributions. In Fig. 5, it is easily noticeable that the maximum of the intensity level averaged profile (solid line) moves towards later phases with respect to the maximum of the mean pulsar profile (dotted line) for both frequencies and the shift increases with frequency from 0.36° at 4.85 GHz to 0.55° at 8.35 GHz. It means that low-intensity single pulses contribute mainly to the leading part of the first component, whereas higher intensity single pulses contribute almost exclusively to its trailing part. On the other hand, the second component is composed mainly of the lowest intensity single pulses – it is visible only in the first two intensity ranges. The shifts of pulsar components were also investigated by Mitra, Rankin & Gupta (2007). They report that the stronger emission of B0329+54 comes earlier than the weaker emission, with a delay of 1.5°. This is opposite to what we have observed. Moreover, Mitra et al. investigated the effect only at one frequency, i.e. 325 MHz. Therefore, further investigations of more pulsar single pulses are highly recommended, because the mechanism behind the observed effect is not understood and we do not know how common it may be in other pulsars.

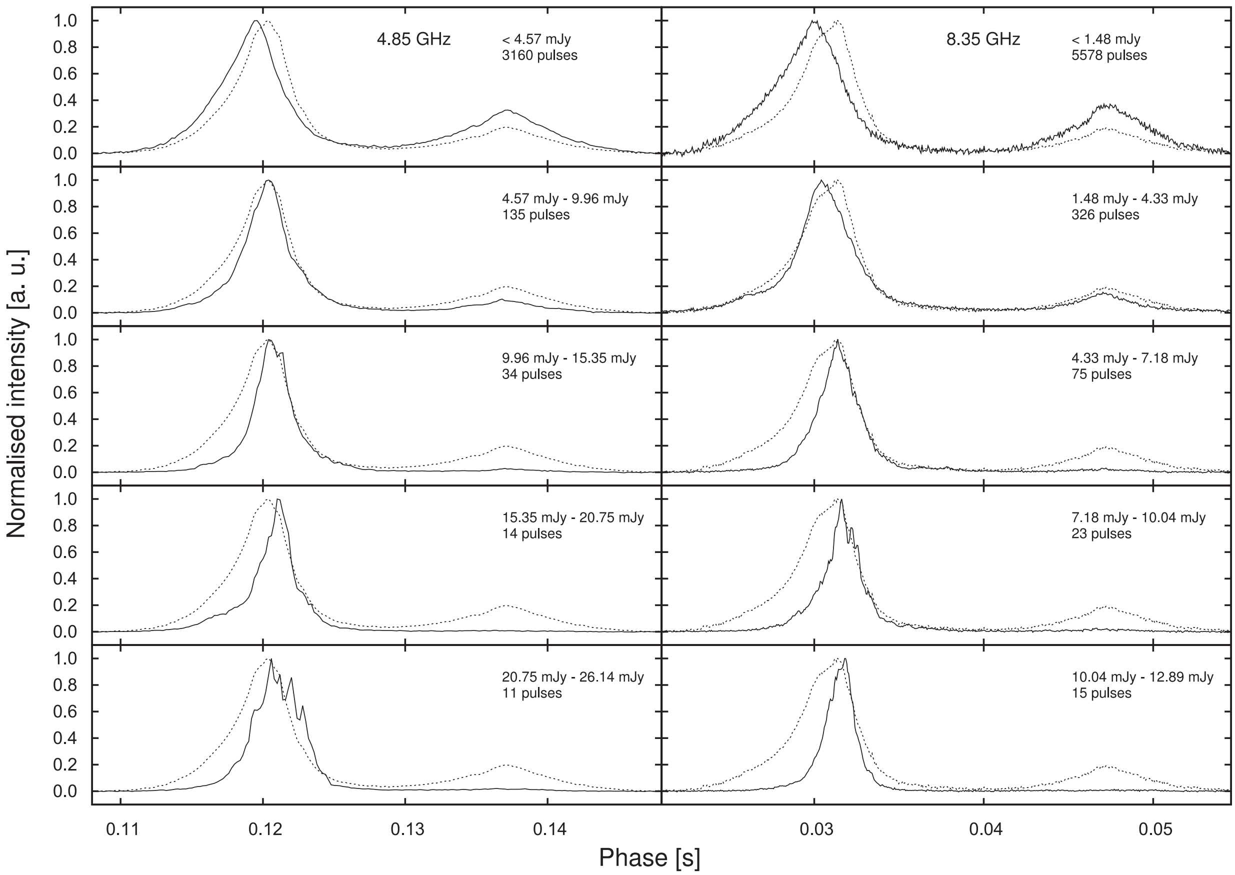

Figure 5. Normalized profiles (solid lines) averaged over first five intensity ranges (see Fig. 4) and the mean profile for all single pulses (dotted line) at 4.85 GHz (left column) and 8.35 GHz (right column).

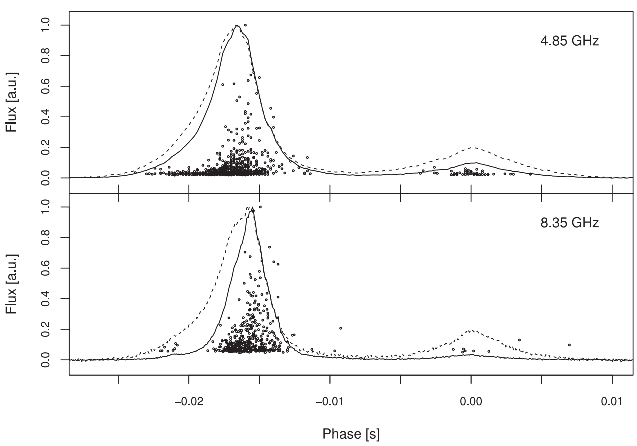

Figure 6. Maximum flux positions for single pulses with SNR > 20σ at 4.85 GHz (top panel) and 8.35 GHz (bottom panel). The mean profile composed of all pulses is plotted with a dotted line, whereas the mean profile composed of the pulses with SNR > 20σ is plotted with a solid line. Both mean profiles and flux maxima of individual pulses are normalized with respect to their maximum values. The profiles are aligned with respect to the maximum of the trailing component at both frequencies.

It is clearly visible in Fig. 6 that, at 4.85 and 8.35 GHz, maximum flux values (denoted with dots) contribute almost exclusively to the trailing edge of the first component of the mean profile, whereas studies at lower frequencies report that the contribution is spread almost uniformly, covering all phases of the pulse mean profile (Karuppusamy, Stappers & Serylak 2011). A mean profile composed only of single pulses with SNR > 20σ is plotted with a solid line, whereas the mean profile composed of all single pulses is plotted with a dotted line. The numbers of such pulses are 758 (23 per cent) at 4.85 GHz and 407 (7 per cent) at 8.35 GHz, respectively.

4 EMISSION HEIGHTS

In the case of 8.35 GHz data from Fig. 5 (right-hand panels), one can read a shift of 0.0018 s ($\Delta\phi \approx 0.55^\circ = 0.001$ rad) between the longitude of the low-flux and high-flux emission. Ignoring (for a while) the curved shape of the B-field lines, this shift can be translated to an altitude difference: $\Delta r_{\rm em} = R_{\rm LC}\Delta\phi/2 = 2.7 \times 10^7$ cm (independent of α and ζ). However, the radius of curvature of B-field lines at the rim of the polar cap of this pulsar is $\rho_{\rm B} = (4/3)(r_{\rm NS}R_{\rm LC})^{1/2} = 10^8$ cm. The upward shift of emission by $\Delta r_{\rm em}$ results, therefore, in a change of emission direction by $\Delta r_{\rm em}/\rho_{\rm B} \approx 0.27$ rad $\approx 15^\circ$, which is much larger than the observed displacement of 0.5°. Therefore, if the observed misalignment of low-flux and high-flux emission has anything to do with the real spatial shift of the emission region, it must be dominated by the effect of curved B-field lines rather than the aberration–retardation shift. Unfortunately, in such a case, full information regarding the geometry is needed to determine $r_{\rm em}$ or $\Delta r_{\rm em}$. The same logic applied to 4.85-GHz data (left-hand panels of Fig. 5) yields the following results: $\Delta\phi \approx 0.36^\circ = 0.006$ rad, $\Delta r_{\rm em} \approx 1.8 \times 10^6$ cm and $\Delta r_{\rm em}/\rho_{\rm B} \approx 10^\circ$, which is also much bigger than the measured shift of 0.36°.

Table 3. Flux density measurements for PSR B1133+16, with references.

Frequency [MHz]	Flux [mJy]	Error [mJy]	Reference	Frequency [MHz]	Flux [mJy]	Error [mJy]	Reference
16.7	310	50	[1]	156	580	58	[1]
16.7	1410	320	[1]	160	520	80	[1]
20	700	100	[1]	170	380	150	[1]
25	560	100	[1]	173.75	380	38	[4]
25	1900	230	[1]	196	560	260	[1]
34.5	900	90	[1]	270	790	190	[1]
39	740	107	[1]	275	475	85	[1]
39	620	90	[2]	341	320	60	[5]
53	1105	260	[1]	370	305	124	[1]
61	830	170	[1]	408	256	53	[6]
61	700	140	[2]	606	144	35	[6]
74	780	150	[1]	626	120	40	[5]
80	640	70	[1]	925	37	11	[6]
80	1000	500	[1]	1400	24.92	15.33	[7]
85	910	150	[1]	1408	32	5	[6]
85	770	130	[2]	1412	60	20	[5]
100	420	150	[1]	1606	51	15	[6]
102	1210	180	[1]	2300	7.07	3.24	[7]
102	1280	550	[3]	2700	8.7	0.6	[7]
102	1520	660	[1]	4850	2.7	1.07	[7]
102	1020	200	[2]	4850	2.4	0.5	[5]
111	770	190	[1]	4850	1.59	0.16	this article
116.75	550	55	[4]	8350	0.73	0.07	this article
130	720	72	[4]	8500	0.86	0.12	[7]
139.75	1000	100	[4]	10550	0.63	0.12	[7]
142.25	1000	100	[4]	14600	0.169	0.0507	[7]
147.5	580	58	[4]	14800	0.26	0.078	[7]
151	1100	170	[1]	24000	0.178	0.0534	[7]
151	805	75	[1]	32000	0.03	0.02	[7]
156	800	80	[4]	32000	0.055	0.06	[8]

References: [1] Malofeev (1999), [2] Izvekova et al. (1981), [3] Malofeev, Malov & Shchegoleva (2000), [4] Karuppusamy et al. (2011), [5] Kramer et al. (2003), [6] Lorimer et al. (1995), [7] Maron et al. (2000), [8] Löhmer et al. (2008).

Using $\alpha = 88^\circ$ and $\beta = 9^\circ$ (Gangadhara et al. 1999) and canonical formulae (Lorimer 2005), we derived radio-emission heights at 4.85 and 8.35 GHz. While making the height estimates, we associate the peak separation with two different sets of B-field lines: the last open field lines, which have the standard magnetic colatitude $\sin\theta_{\rm pc} = (r_{\rm NS}/R_{\rm LM})^{1/2}$, and the critical field lines, which have $\sin\theta_c = (2/3)^{3/4}(r_{\rm NS}/R_{\rm LC})^{1/2}$.

Simple calculations yield estimations of the emission heights at 4.85 GHz of 67×10^6 and 122×10^6 cm for the last open and critical magnetic field lines, respectively, whereas for stronger emission they are closer to the neutron star surface at 66×10^6 and 120×10^6 cm. Similarly, at 8.35 GHz, emission heights are 66×10^6 and 122×10^6 cm for the last open and critical field lines, respectively, whereas for stronger emission they are 65×10^6 and 119×10^6 cm. Our analysis shows that the emission region is located at a distance of around 1–2 per cent of the light-cylinder radius from the pulsar surface, which is consistent with earlier studies (e.g. Krzeszowski et al. 2009).

5 RADIO SPECTRUM

In general, pulsars have steep spectra with an average spectral index around −1.8 (Maron et al. 2000). Aside from the basic spectrum (which can be described with a power law $S \propto \nu^\alpha$), there are two common types: a spectrum with a break (described with two power laws) and a spectrum with a turn-over (clearly visible maximum flux). We collected flux density measurements from different publications (Table 3). Our data set covers a very wide radio frequency range from 16.7 MHz up to 32 GHz. The analysis of the data presented in this article yielded mean flux values of 1.59 and 0.73 mJy at 4.85 and 8.35 GHz, respectively, with an estimated error of 10 per cent of the original value. The spectrum of PSR B1133+16 spanning a wide radio frequency range is shown in Fig. 7. Each point denotes a measurement of mean flux density with its respective uncertainties. We included measurements by Karuppusamy et al. (2011) at seven frequencies, ranging from 116.75–173.75 MHz. The authors claim that the spectrum of PSR B1133+16 over their 'reasonably wide frequency range' of 57 MHz is of a broken power-law type with spectral indices of $\alpha_1 = 2.33 \pm 2.55$ and $\alpha_2 = -3.8 \pm 2.24$. In Fig. 7, we have indicated their spectrum by a dashed line. We cannot confirm Karuppusamy's spectral indices, which were obtained from low-frequency measurements covering only a small range of frequencies. However, we find that Karuppusamy's measurements have a typical spread of flux values and thereby fit well into the overall spectrum, as can be seen in Fig. 7.

Our spectrum of PSR B1133+16 may be described by two power laws over the whole frequency range, with $\alpha_1 = -0.04 \pm 0.0001$ and $\alpha_2 = -1.96 \pm 0.0001$ with a break frequency of $\nu_{\rm b} = 256 \pm 0.016$ MHz ($\chi^2_{\rm red} = 5.1$).

To reproduce the spectrum of PSR B1133+16 covering a 32-GHz frequency range, we have also fitted the flicker-noise model

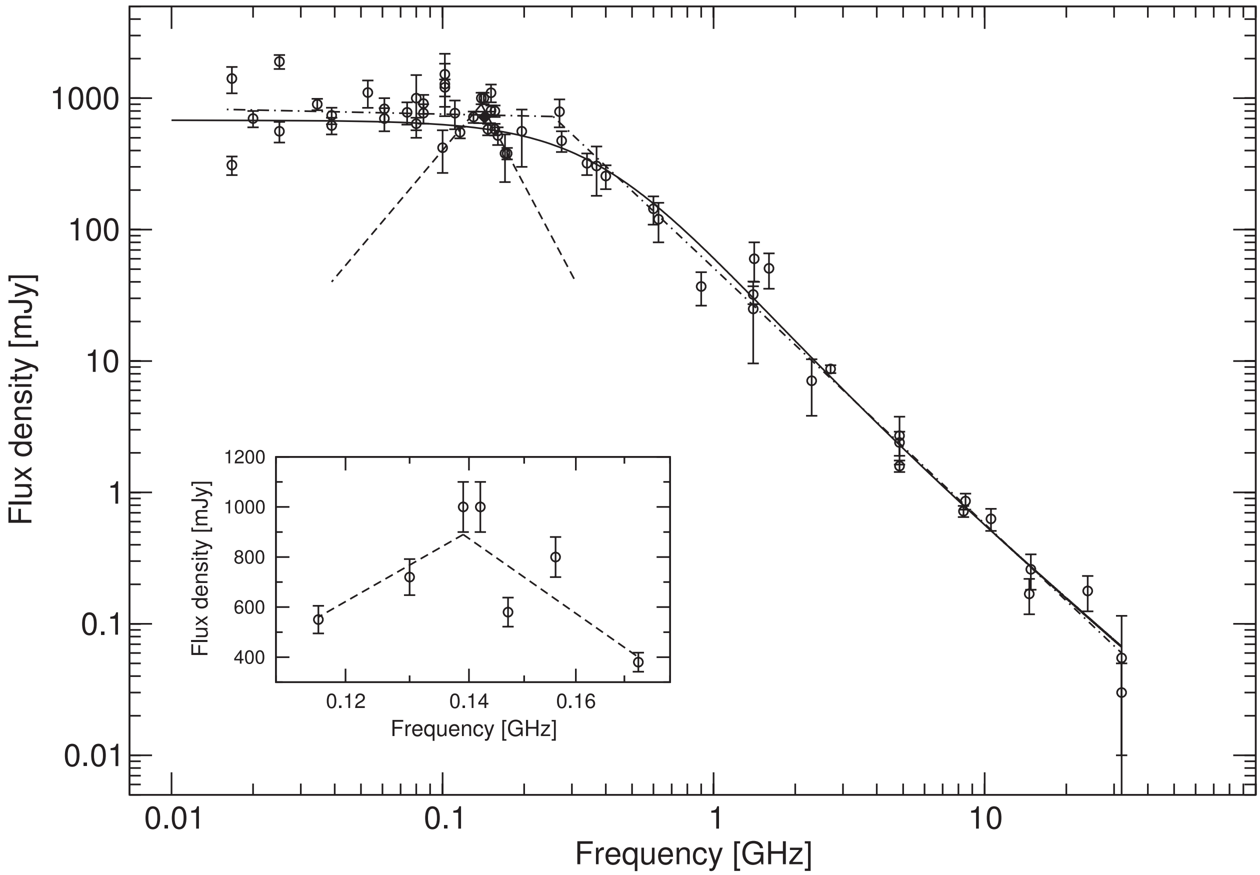

Figure 7. Spectrum of PSR B1133+16. Individual measurements are listed in Table 3. The inset contains the spectrum (dashed line) as presented in Karuppusamy et al. (2011). The solid line represents a fitted model using equation (3) (Löhmer et al. 2008). The dot–dashed line represents a broken power-law fit. See the text for details.

proposed by Löhmer et al. (2008), which is described by

$$S(\omega) = S_0 \left(\frac{1 + \omega^2 \tau_e^2}{\tau_e^2} \right)^{n-1} \times \mathrm{e}^{-\mathrm{i}(n-1)\mathrm{atan}(\omega\tau_e)}, \tag{3}$$

where S_0 is a scaling factor, $\omega = 2\pi\nu$, ν is an observing frequency, τ_e is a characteristic time for nanoburst decay and n is an exponent that constrains a combination of physical parameters of nanopulses (for details refer to Löhmer et al. 2008). Our fitted parameters of $S_0 = 3.39 \pm 0.77$ Jy, $\tau_e = 0.40 \pm 0.05$ ns and $n = 0.118 \pm 0.022$ are in good agreement with the result of Löhmer et al. (2008) and our reduced $\chi^2_{\mathrm{red}} = 4.7$ is comparable to the value for the broken power-law fit. The model, apart from the scaling factor S_0, is based on only two physical parameters. The first is the duration of a nanopulse (τ_e) and the second (n) is related to the geometry of the emission process. It is based on the assumption that the pulsar radio emission is in fact the superposition of many nanopulses, which in the case of PSR B1133+16 have durations of $\tau_e = 0.51$ ns according to Löhmer et al. (2008). However, our fit gives an even shorter nanopulse duration of 0.4 ns. Löhmer et al. (2008) report that, for 12 pulsars, $0.1 < \tau_e < 2.0$ ns.

6 CONCLUSIONS

Analysis of single pulses of PSR B1133+16 is a process that needs a certain amount of care. First of all, it is important to take into account different observational and technical effects that can affect recorded data, especially those with very high time resolution. The effects that are presented in this article play a huge role and alter the data significantly. An understanding of such effects and their influence on the data recording process is important for proper data reduction. Some of the effects are not visible in mean profiles, but only in single pulse data.

The mean profiles of PSR B1133+16 at 4.85 and 8.35 GHz consist of two components (Fig. 2). The second component is emitted almost exclusively by low-intensity individual pulses. On the other hand, the first component is seen in single pulses regardless of their intensity, except for cases in which it is not present at all. However, lower intensity emission contributes mostly to the leading part of the first component, whereas higher intensity single pulses contribute mainly to its trailing part (Fig. 5), something also reported by Maron et al. (2013). The results of analysis of 4.85- and 8.35-GHz data are consistent with previous studies by (Nowakowski 1996) at 430 MHz, but studies of B0329+54 (Mitra et al. 2007) show entirely opposite behaviour without a full explanation. This inconsistency requires further studies of single pulses of other pulsars to explain the effect.

We show, in contradiction to studies at lower frequencies by Karuppusamy et al. (2011), who report an almost uniform spread of single pulse maxima, that the maximum emission of B1133+16 single pulses at 4.85 and 8.35 GHz contributes almost exclusively to the trailing part of the leading component of the mean profile. Our result is consistent with the behaviour at 341, 626, 1412 and 4850 HMz mentioned by Kramer et al. (2003) and extends the studies up to 8.35 GHz.

Radio emission arises close to the pulsar surface at distances of around 65 stellar radii at frequencies of 4.85 and 8.35 GHz. Weaker emission, which contributes to the leading part of the leading components, comes in earlier phases, which suggests that it originates in the magnetosphere, further from the pulsar surface than more energetic emission. Our calculations show that the difference in emission heights for stronger and weaker emission is of the order of a few stellar radii, amounting to a change of 1–2 per cent in the emission height, which is consistent with previous estimations (Krzeszowski et al. 2009).

There are 60 mean flux measurements for PSR B1133+16 in the literature that are known to us. They span a very wide radio frequency range, from 16.7 MHz up to 32 GHz. To reproduce the spectrum, we fitted two different models: the broken power-law model and a model based on the flicker-noise model of pulsar radio emission (Löhmer et al. 2008). Surprisingly, the model proposed by Löhmer et al. (2008) is not widely used in the literature, although it reproduces the pulsar spectrum comparably well to the power-law model. Future high time resolution observations might be useful to verify the nanopulse emission model.

Due to the fact that the pulsar radio emission is weaker at higher frequencies, giant pulses are the ones that allow us to study their structure closely. In both our data samples, roughly 1 per cent of bright pulses are at least ten times stronger than the mean flux and their microstructure is clearly visible.

ACKNOWLEDGEMENTS

The results presented are based on observations with the 100-m telescope of the Max-Planck-Institut für Radioastronomie (MPIfR) at Effelsberg. This work has been supported by Polish National Science Centre grants DEC-2011/03/D/ST9/00656 (KK, AS), DEC-2012/05/B/ST9/03924 (OM) and DEC-2011/02/A/ST9/00256 (JD). Data analysis and figures were partly prepared using R (R Core Team 2013).

REFERENCES

Brisken W. F., Benson J. M., Goss W. M., Thorsett S. E., 2002, ApJ, 571, 906
Crossley J. H., Eilek J. A., Hankins T. H., Kern J. S., 2010, ApJ, 722, 1908
Dyks J., Rudak B., 2012, MNRAS, 420, 3403
Dyks J., Rudak B., Demorest P., 2010, MNRAS, 401, 1781
Ferguson D. C., Seiradakis J. H., 1978, A&A, 64, 27
Gangadhara R. T., Xilouris K. M., von Hoensbroech A., Kramer M., Jessner A., Wielebinski R., 1999, A&A, 342, 474
Izvekova V. A., Kuzmin A. D., Malofeev V. M., Shitov I. P., 1981, A&AS, 78, 45
Jackson J. D., 1975, Classical Electrodynamics. Wiley, New York
Kargaltsev O., Pavlov G. G., Garmire G. P., 2006, ApJ, 636, 1139
Karuppusamy R., Stappers B. W., Serylak M., 2011, A&A, 525, 13
Kramer M., Karastergiou A., Gupta Y., Johnston S., Bhat N. D. R., Lyne A. G., 2003, A&A, 407, 655
Krzeszowski K., Mitra D., Gupta Y., Kijak J., Gil J., Acharyya A., 2009, MNRAS, 393, 1617
Lange C., Kramer M., Wielebinski R., Jessner A., 1998, A&A, 332, 111
Löhmer O., Jessner A., Kramer M., Wielebinski R., Maron O., 2008, A&A, 480, 623
Lorimer D., 2005, Handbook of Pulsar Astronomy, Cambridge Observing Handbooks for Research Astronomers. Cambridge University Press, Cambridge
Lorimer D. R., Yates J. A., Lyne A. G., Gould D. M., 1995, MNRAS, 273, 411
Malofeev V. M., 1999, Katalog radiospektrov pul'sarov, Pushchino:PRAO
Malofeev V. M., Malov O. I., Shchegoleva N. V., 2000, Astron. Rep., 44, 436
Manchester R. N., Hobbs G. B., Teoh A., Hobbs M., 2005, AJ, 129, 1993
Maron O., Kijak J., Kramer M., Wielebinski R., 2000, A&AS, 147, 195
Maron O., Serylak M., Kijak J., Krzeszowski K., Mitra D., Jessner A., 2013, A&A, 555, A28
Mitra D., Rankin J. M., Gupta Y., 2007, MNRAS, 379, 932
Nowakowski L. A., 1996, ApJ, 457, 868
R Core Team, 2013, R: A Language and Environment for Statistical Computing. R Foundation for Statistical Computing, Vienna
Zharikov S., Mignani R. P., 2013, MNRAS, 435, 2227
Zharikov S. V., Shibanov Y. A., Mennickent R. E., Komarova V. N., 2008, A&A, 479, 793

This paper has been typeset from a TEX/LATEX file prepared by the author.